CrystEngComm

Accepted Manuscript

ROYAL SOCIETY OF CHEMISTRY

www.rsc.org/crystengcomm

Journal Name

ARTICLE

Tuning the optical, electronic and luminescent properties of LaOCl:Eu^{3+} via structural and lattice strain modulation

Received 00th January 20xx,
Accepted 00th January 20xx

DOI: 10.1039/x0xx00000x

www.rsc.org/

Li Lv,[ab] Ting Wang,[a] Sipeng Li,[a] Yiguo Su[a] and Xiaojing Wang*[a]

In this work, LaOCl:Eu^{3+} nanodisks have been successfully synthesized by hydrothermal process followed by a subsequent heat treatment process. It is observed that the monotonous lattice contraction originated from the incorporation of Eu^{3+} into LaOCl host matrix has consequence on the structural variation and lattice strain modulation. Meanwhile, the lower Eu^{3+} doping content can induce the band gap narrowing of LaOCl, which is further confirmed by density function (DFT) results. However, different to theoretical predictions, Eu^{3+} doped LaOCl nanodisks show the constantly narrowing band gap energy with increasing Eu^{3+} doping concentration determined by UV–vis diffuse reflectance spectra, which are thought to be related to the increase of lattice strain. Futhermore, the Eu-O charge transfer band shifts to low energy in excitation spectra with the increasing Eu^{3+} ions doping concentration, which can be attributed to strengthen the covalence of Eu–O bonds in the crystal structure environment of LaOCl host matrix. For Eu^{3+} doped LaOCl system, the luminescent intensity is influenced by the concentration quenching as well as the lattice strain. LaOCl:Eu^{3+} nanodisks exhibit good red emission property with a maximized quantum efficiency of 87.4%. Thus, it is expected the luminescent colors of Eu^{3+} doped LaOCl samples can be tuned by simply adjusting the relative doping concentration of Eu^{3+} ions, which might find potential applications in the fields such as light display systems and optoelectronic devices.

Introduction

As one of the most important luminescent phosphors, lanthanum oxyhalide is of interest for displays, up-conversion lasers, and other related optoelectronic devices. [1-3] Generally, lanthanum oxyhalide is used as a potential host, because La^{3+} ion has the largest ionic radius among lanthanide series of ions substituted by other different rare earth ions (Ln^{3+} ions) as luminescent activators. [4-6] Moreover, lanthanum oxyhalide has unique and excellent characteristics, such as high chemical stability, low maximum phonon cut off energy, and efficiently transfer phonon energy to dopant ions. [7, 8] Therefore, lanthanum oxyhalide doped with the rare earth ions plays an important role in luminescent application field. [9-11] Till now, a great amount of strategies have been developed to enhance the rare earth ions doped lanthanum oxyhalide luminescent efficiency with well-designed crystal structure, chemical compositions, morphologies for improving luminescent efficiencies to meet the wide requirement. [12-18] Although many phosphors for the stratagem are currently available, red phosphors still have to be improved for their efficiency, thermal and chemical stability. Thus, the development of new red phosphors, which can be excited efficiently by near-UV chips, is the research focus recently.

It has been generally accepted that microstructure variation has important influenced on luminescent materials properties. [12-14, 19] Among which, lattice strain plays an important role in determining the properties of material. Much higher strain can be tolerated in nanocrystals than their bulk counterparts. Therefore, the special behaviour induced by lattice strain has gained great interest for function material on the nanometre scale.[19-22] Generally, in crystalline solids, dopant ions substituted metal ions of the host lattice often leads to the lattice distortion. The strain arisen from lattice mismatch can modify the energy levels of the bonding electrons. Therefore, the lattice strain cause the variation of the photoluminescent intensity.[23-26] For luminescent materials, strain is expected to tune the optical and luminescent properties. It is found that the strain-tuneable nanostructures show a narrow light emission with high quantum efficient to expect to have application in solar energy conversion, multicolour biomedical imaging and super-resolution optical microscopy.[23] The quantum yield had been significantly enhanced for upconversion nanoparticles due to lattice strain. [27] It is found

[a] College of Chemistry and Chemical Engineering, Inner Mongolia University, Hohhot, Inner Mongolia, 010021, P. R. China.
[b] College of Chemistry and Chemical Engineering, Inner Mongolia University of Technology, Hohhot, Inner Mongolia, 010051, P. R. China.

Electronic Supplementary Information (ESI) available: [details of XRD patterns of LaOCl:Eu^{3+} sample (x = 0.079) and complete crystal sample (Fig. S1), the crystallinity of LaOCl:Eu^{3+} nanodisks (Table S1), the relationship between initial molar ratio and measurement molar ratio of LaOCl:Eu^{3+} nanodisks (Table S2), Rietveld refined X-ray diffraction patterns of the Eu^{3+} doped LaOCl nanodisks (Fig. S2), Rietveld refinement parameters for Eu^{3+} doped LaOCl nanodisks using GSAS program (Table S3), Band structures of LaOCl:Eu^{3+} nanodisks (a) x= 0.0417, (b) x= 0.0625, (c) x= 0.125, (d) x= 0.25(Fig. S3), TG curves of LaOCl:Eu^{3+} nanodisks (Fig. S4), Parameters obtained from double-exponential fitting to the decay data of Eu^{3+} doped LaOCl nanodisks (Table S4), CIE values and R/O values of LaOCl:Eu^{3+} nanodisks (Table S5)]. See DOI: 10.1039/x0xx00000x

that the emission intensity of doped materials, in particularly rare earth ions doped nanocrystals increase with decreasing the tensile lattice strain and with increasing compressive strain due to the surface-related effects.[28] Lattice strain resulted in variation of luminescent property in decay time, quantum efficiency, and nonradiative transition for $LaPO_4$:Yb/Tm nanocrystals.[29]

In this work, a series of Eu^{3+} doped LaOCl with different Eu^{3+} concentration were firstly synthesized via two step reactions consisting of the hydrothermal method accompanied by post annealing. On the base of experimental and theoretical results, the impact of Eu^{3+} ions on structural parameters, lattice strain and optical properties has been systematic studied. The influence of the lattice strain on the luminescent property induced by Eu^{3+} doping was investigated. The present result will give a foundation theory research to develop the luminescent property of lanthanum oxyhalide.

Experimental section

The samples of LaOCl:Eu^{3+} nanocrystals were prepared by a hydrothermal treatment followed by calcination. The synthetic procedure for Eu^{3+} doped LaOCl nanocrystals can be briefly described as follows: Firstly, 1g of polyvinyl pyrrolidone (PVP) was dissolved in 35 mL of ethanol solution, 5 mmol of $LaCl_3 \cdot 2H_2O$ and the different contents of $EuCl_3$, with the molar ratio of Eu/La was fixed to be 0, 0.02, 0.04, 0.06, 0.08, 0.10, 0.12, 0.15, 0.20, 0.30, were added into the above-mentioned mixed solvent with magnetic stirring. Subsequently, 35mL of 0.08 mol/L ammonia solution was added dropwise into the solution to form white precipitate. Then, the mixture was transferred into a 100 mL Teflon-lined stainless autoclave and reacted at 160 ºC for 24 h. The resultants were separated by centrifugation and dried at 60 ºC for 4 h to obtain the powder precursors. Finally, the calcinate treatment was carried out for powder precursors in a muffle furnace at 250 ºC for 2 h and then 600 ºC for 4h. After cooling to room temperature, the samples were washed with distilled water several times and dried at 60 ºC for 4 h.

Phase compositions of the samples were characterized by powder X-ray diffraction (XRD) at room temperature on Rigabu DMAX2500 X-ray diffractometer with a copper target (Cu Kα, λ=0.15406 nm). The scanning electron microscopy (SEM) images were measured by HITACHI S-4800 at the accelerating voltage of 5 kV. Transmission electron microscopy (TEM) and high resolution transmission electron microscopy (HRTEM) images were tested using an FEI Tecnai G^2 F20 S-TWIN apparatus operated at 200 kV. Energy-dispersive X-ray (EDX) pattern was obtained using GENESIS energy dispersive X-ray apparatus (EDAX). Chemical compositions of the samples were quantitatively determined using inductive coupled plasma optical emission spectroscopy (ICP) on a Perkin–Elmer Optima 7000DV instrument. Optical diffuse reflectance spectra of the samples were measured using UV-3600 spectrometer (Simadzu). $BaSO_4$ was used as a reference material. The Fourier transform infrared (FT-IR) spectra of the samples were obtained on a Perkin-Elmer IR spectrophotometer at a resolution of 4 cm^{-1} using KBr pellet technique. The photoluminescence (PL) excitation and emission spectra and transient decay were taken on Edinburgh Instruments FLS920 time-resolved fluorescence spectrometer equipped with both continuous (450 W) and pulse xenon lamps.

Calculations of the Electronic Band Structure

The electronic structures of the samples were calculated using plane-wave based density functional theory with the CASTEP program package. The ionic cores of the elements were represented by scalar relativistic, fully separable, ultrasoft pseudopotentials. The generalized gradient approximation (GGA-PBE) was applied, and the kinetic energy cutoff was selected at 430 eV. Eu^{3+} ions were partly substituted by La^{3+} ions in the LaOCl cell to simulate the Eu^{3+} doped LaOCl system. The compositions used for the calculation were pure LaOCl and LaOCl: xEu^{3+} (x = 0.0417, 0.0625, 0.125 and 0.25 mol %).

Results and discussion

The morphologies of the prepared samples were examined by TEM. It was observed that the sample of Eu^{3+} doped LaOCl (x = 0.079) exhibited a disk-like shape in Fig. 1a, the demensions of disks was about 60 nm. As seen in Fig. 1b, the corresponding high-resolution TEM image of Eu^{3+} doped LaOCl (x = 0.079) nanodisks present a well-resolved fringe of the tetragonal LaOCl crystal. The lattice fringes of 0.351, 0.206, and 0.296 nm are assigned to the (101), (200) and (110) planes of the tetragonal LaOCl crystal, respectively. The chemical composition of the synthesized materials was measured by EDX analysis. A typical EDX data of Eu^{3+}-doped LaOCl nanocrystals (x = 0.079) sample (Fig. 1c) confirmed the presence of La, Cl, O, and Eu elements.

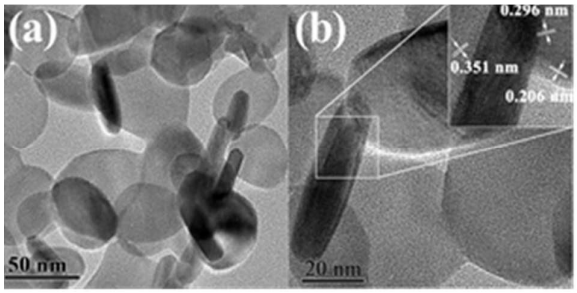

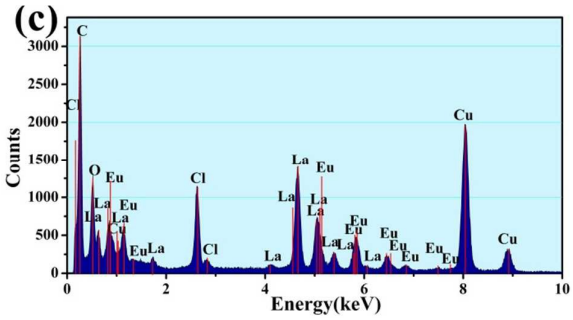

Fig. 1 TEM image (a), high-resolution TEM image (b) and EDX data (c) of Eu^{3+} doped LaOCl nanodisks (x = 0.079).

The phase structures of the prepared samples were examined by XRD. As shown in Fig. 2a, all XRD diffraction peaks of the as-obtained sample can be indexed to tetragonal phase LaOCl (JCPDS No. 01-088-0064). No traces of impurity peaks from the other phases was observed, confirming that the samples were a single tetragonal phase. The XRD diffraction peaks for Eu^{3+} doped LaOCl showed no noticeable variation in comparison to the pure tetragonal LaOCl, indicating the Eu^{3+} ions well dispersed in the LaOCl nanocrystals. Moreover, when the dopant concentration of Eu^{3+} was even up to 0.30, no reflection was detected, confirming neither the formation of Eu_2O_3 nor impurities phase. All of the samples crystallized after calcination under the same prepared condition, XRD pattern of the samples of LaOCl:Eu^{3+} nanodisks showed similar peak intensity to the pure samples as seen in Fig. 2(a). The crystallinities of the samples were calculated listed in Table S1. Complete crystal sample was obtained by calcining pure LaOCl sample at 1000 ºC for 48 h. XRD pattern was shown in Fig. S1. The crystallinity of the samples increased with Eu^{3+} concentration to show a maximum value 50.46% at x = 0.04, whereas further increasing the Eu^{3+} concentration led to a slightly decrease. The diffraction peak of (101) was obviously observed systematically shift to high angle with the increasing doping concentration of Eu^{3+} ions (Fig. 2b). It is originated from the substitutions of the slightly larger La^{3+} ions (1.16 Å) by the smaller of Eu^{3+} ions (1. 066 Å), confirming the Eu^{3+} ions were well stabilized in La^{3+} sites in the LaOCl crystal lattices.[26-28] To prove the presence of Eu^{3+} in LaOCl nanodisks, chemical analyses of the as-prepared samples were also performed by ICP-OES technique. As indicated in Table S2, the final molar ratios of Eu^{3+} contents in LaOCl nanodisks increased with the initial Eu^{3+} concentration while they were all smaller than the initial ones.

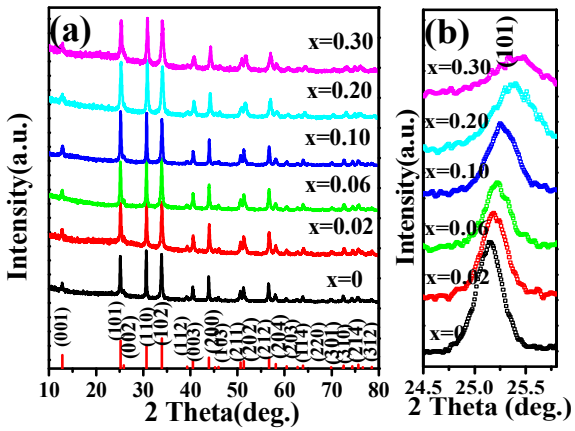

Fig. 2 (a) XRD patterns of LaOCl:Eu^{3+} samples with different dopant concentration of Eu^{3+}. Vertical bars at the bottom denote the standard data for a tetragonal PbFCl structure of bulk LaOCl (JCPDS, No. 01-088-0064), (b) Enlarged diffraction lines for Eu^{3+} doped LaOCl nanodisks in a narrowed angle range from 24.5 to 25.8º.

The variation of the lattice parameter would result in the shift of 2θ according to Bragg's law, the refined lattice parameters of the samples were obtained by a least-squares method using GSAS software.[30] As shown in Fig. 3, all structural parameters were strongly depended on the dopant concentration (x) of Eu^{3+} ions: the a-axis (lattice parameter a = b) length decreased linearly from 4.120 to 4.072 Å with increasing x. Meanwhile, the variation of c-axis length followed a similar trend, which was shorten from 6.883 to 6.836 Å. As a consequence, the unit cell volumes declined linearity with the increasing dopant content of Eu^{3+} ions. The variations of lattice parameters for Eu^{3+} doped LaOCl sample were specify the homogeneous incorporation of Eu^{3+} into the LaOCl host matrix. As observed in Fig. S2, the simulated XRD patterns matched the experimental data well. Moreover, fit parameters, R_p and R_{wp}, standing for the regression sum of relative errors and the regression sum of weighted squared errors, were extremely small (fitting parameter R_p, R_{wp}, and χ^2 are listed in Table S3). Thus, the above mentioned results were highly satisfactory reliability.

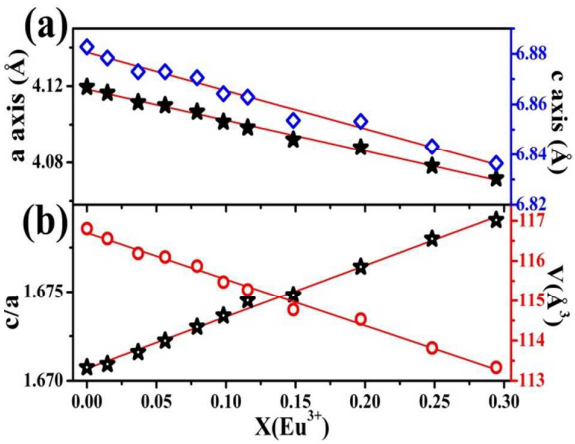

Fig. 3 (a) Lattice parameters (a and c), (b) axial ratio of c/a and unit cell volume are given as a function of dopant level forEu^{3+}.

The impact of doping Eu^{3+} on structural properties should be emphasized because of the following considerations. It was well-known that the lattice parameter and unit cell volume could be influenced by two major factors, including size effect and doping effect. [31-33] According to previous literatures, larger particle size of nanoparticles leads to less lattice parameter variation. [31-33] The diameters for the majority of particles were about 60 nm in the present samples. Thus, size effect could not be a dominant factor. In addition, for LaOCl:Eu^{3+} nanodisks, the variations of lattice parameters are well linearly related to the doping concentration. Based on all above analysis, we proposed the doping effect is a dominantly factor for the variation of structure in the present system. In the Eu^{3+} doped LaOCl system, due to the same valence state, similar ions radius and properties between Eu^{3+} and La^{3+} ions, the Eu^{3+} ion would be easily introduced into the LaOCl host matrix to substitute La^{3+} ion site. The lattice contraction was produced because the radiu of Eu^{3+} ion was 1.066 Å which was smaller than that of La^{3+} (1.16 Å). A larger lattice distortion appeared and the trend increased with the Eu^{3+} doping concentration increasing. The similar phenomenon had been reported for several oxide nanocrystals. [34, 35] Therefore, it was concluded the lattice structure of LaOCl:Eu^{3+} nanodisks could be effectively tuned by doping Eu^{3+} ion with a suitable content.

Interestingly, we found that the linear relations existed between the axial ratio of c/a and the Eu^{3+} doping concentration. The axial ratio c/a of bulk LaOCl (JCPDS no. 01-088-0064) was 1.6701 by DFT calculation. However, the values were at the range of 1.6707-1.6790 for Eu^{3+} doped LaOCl by XRD calculation, obviously larger than the tetragonal bulk structure. Moreover, this lattice structure distortion was more and more serious with the doping concentration increased. It was reported that the high doping concentration would give rise to abundant defect centers, resulting in the reduced structure symmetry and the disturbed local structure. [35, 36] In the case of LaOCl crystal, it is a layer structure with the alternated $(LaO)_n^{n+}$ cation and Cl^- anion layers along the crystallographic c axial direction, in which La atoms are located between layers surrounded by four O atoms and five Cl atoms (four O atoms in the same layer, other Cl atom in the next layer). [37] When the alien atoms (Eu ions) are doped into LaOCl host matrix, the lattices are inevitably misplaced with a real lattice structure, particularly O and Cl atoms site. It is confirmed by the structural refinement results that the band lengths of La(Eu)-O vary from 2.3973 Å to 2.3631 Å as the dopant level increases from x = 0 to x = 0.294. The dislocation of dopant ions in the host crystal structure would also lead to short-range disordered state and subsequent lead to the diffraction peak broadening. [38] The broadening phenomenon was observed in XRD patterns in Fig. 2b. Generally, the broadening of the diffraction peaks depended upon two predominant factors including strain and particle size. [14, 39, 40] The particle sizes of the Eu^{3+} doping LaOCl nanocystals are about 60 nm with a small change for the various Eu ions doping concentration. Thus the variation of particle size was ruled out from the predominant factors for the disordered structure. It is speculated that the disordered structure may be significantly impacted by the lattice stain.

The lattice stain is calculated by broadening effects of diffraction peaks using Williams and Hall theorem, [33, 41]

$$\beta cos\theta/\lambda = 1/D + \eta sin\theta/\lambda \quad (1)$$

where β is the full width at half-maximum (FWHM), ϑ is the diffraction angle, λ is the X-ray wavelength, D is the effective particle size, and η is the effective strain. The lattice strain was calculated from the slope of a plot $\beta cos\vartheta/\lambda$ *vs.* $sin\vartheta/\lambda$. Fig. 4a showed the relationship between $\beta cos\vartheta/\lambda$ and $sin\vartheta/\lambda$ for Eu^{3+} dopant concentration x = 0.148 of the LaOCl:Eu^{3+} nanodisks. The positive tensile strain of 2.11% was observed. As shown in Fig. 4b, the lattice strain increased from 0.677% to 3.23% with the increases dopant concentration of Eu^{3+}, indicating the enhancement of the lattice distortion of LaOCl:Eu^{3+} nanodisks. It was reported that the different shapes would result in the various lattice strain. [14, 24] Therefore, in the present system, it is necessary to consider whether the sharp or doping play more important influence on strain. The morphologies of LaOCl:Eu^{3+} nanoparticles were examined by SEM, which are represented in Fig. 5. It can be seen that uniform disk shape with a dimensional size was about 75 nm for the pure LaOCl sample. The thickness of the nanodisks was about 20 nm (Fig 5a, 5b). As shown in Fig. 5c-5h, the morphologies of nanodisks remained the same for the Eu^{3+} doping concentration increaseed. Only, the nanodisks diameter decreased slightly from 75 to 55 nm. It was concluded that the strain variation may not originated from the factor of shape change. Therefore, it is proposed the doping effect of Eu^{3+} ions was primarily responsible for the development of strain in LaOCl lattice structure. That is, the contraction in unit cell volume with the Eu^{3+} dopant level increased led to the introduction of the strain in the LaOCl lattice. The similar observation had been reported in Mn-doped SnO_2 nanocrystals. [26]

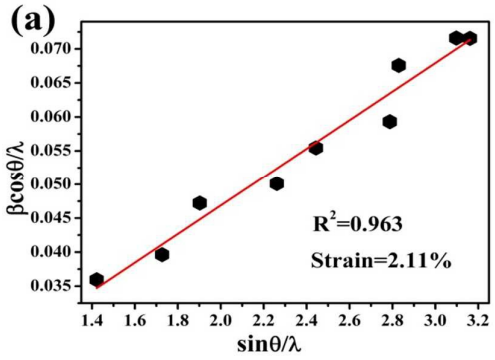

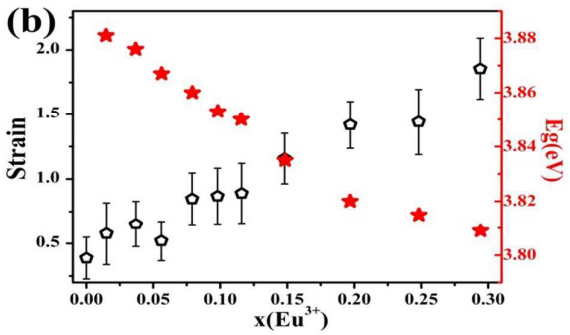

Fig. 4 Relationship (a) between (βcos θ)/λ and (sin θ)/ λ for the samples of LaOCl:Eu^{3+} (x=0.148) and (b) between lattice strain, band gap and Eu^{3+} doped concentration.

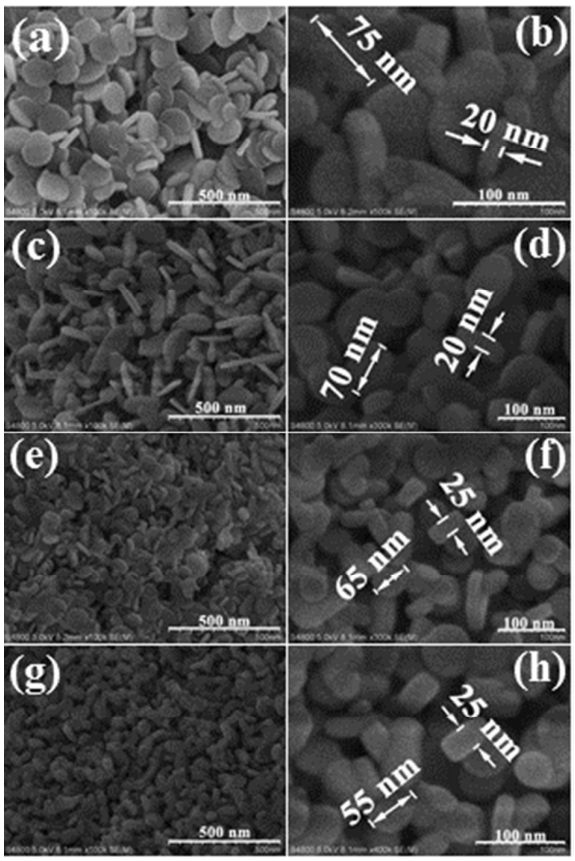

Fig. 5 SEM images of the Eu^{3+} doped LaOCl nanodisks. (a) (b) x = 0, (c)(d) x = 0.056, (e)(f) x= 0.098, (g)(h) x = 0.294.

The UV–vis absorption spectra of Eu^{3+}-doped LaOCl were investigated to study the change of LaOCl energy band structure. The absorption spectrum of the pure LaOCl nanopowders was not observed range from 200 to 600 nm at room temperature in Fig. 6a, which was in accordance with 5.53 eV of the previous reference. [42] There was a new broad adsorption band in the range of 210-350 nm for the Eu^{3+} into LaOCl nanodisks, being related to the typical electronic transition from the O 2p to the Eu^{3+} 4f orbital. A series of absorption peaks ranged from 300 to 600 nm, which were corresponded to the Eu^{3+} f-f transitions.

Basically, the optical band gap near the band edge of a crystalline semiconductor can be described as follows: [43]

$$\alpha h\nu = A(h\nu - E_g)^{n/2} \quad (2)$$

where α, ν, E_g, A, and n are the absorption coefficient, incident light frequency, band gap, constant, and an integer, respectively. The value of n was set as 1 for LaOCl which was assumed to be a direct optical transition semiconductor. The band gap of pure LaOCl sample was 5.53 eV. As shown in Fig. 6b, the band gap of LaOCl: Eu^{3+} sample was 3.88 eV for x = 0.015 and continuously declined down to 3.81 eV for x = 0.294. Several factors are responsible for this band edge shifted to low energy, including doping effect, lattice structural modifications, lattice strain, and so forth. [36, 44] To understand the doping effect of Eu^{3+} on band structure modification of LaOCl, the band structure and partial density of states (DOS) for LaOCl and Eu^{3+} doped LaOCl were calculated on the basis of DFT. On the grounds of tetragonal LaOCl unit cell, a supercell containing 288 atoms was employed for pure LaOCl. A series of models with the different doping ratio based on this supercell were constructed, just by substituting different ratio La atoms by Eu atoms. The structures of all simulated models were stable, and energetically convergent. It was noted that LaOCl has a direct transition feature from the band structure of pure LaOCl nanodisks in Fig. 7, which was verified the above suppose. The band structure of Eu^{3+} doped LaOCl samples were shown in Fig. S3. As shown in Fig. 8a, it was seen that the minimum conduction band of pure LaOCl consisted of La 5d and O 2p hybrid orbital in the energy from 3.88 to 10.80 eV, which La 5d was contributed more electrons, while the maximum valence band consisted of mainly O 2p orbital. The optical band edge was originated from the electronic transition between O 2p and La 5d orbital. The band gap energy for pure LaOCl was calculated to be 4.17 eV, smaller than that of 5.53 eV for LaOCl host lattice measured by UV-vis diffuse spectrum. [42] Though the calculated value using Castep program is slightly larger than experimental data, it still acts as a useful tool to depict the electronic structures of semiconductors due to the fact that only relative positions of the occupied and empty orbital are considered. As illustrated in Fig. 8b, when one La atom was substituted by Eu atom in the LaOCl supercell, it was observed that the conduction bands mainly composed of the La 5d orbital and the valence bands mainly of O 2p orbital were simultaneously shiftd to lower energy. The conduction band shiftd from 4.58 to 3.38 eV, and the valence band shiftd from 0.41 to -0.78 eV. A new impurity band belonged to Eu 4f orbital was observed, range from -0.71 to 1.11 eV between the conduction band and valence band. The appearance of new electronic band obviously led to band gap narrowing of LaOCl: Eu^{3+} compared with pure LaOCl. However, it was interestingly observed from Fig. 8c, 8d and 8e that the narrowing of the band gap kept to be constant for LaOCl: Eu^{3+} nanodisks although the Eu^{3+} doping contents variation. It was not compatible with the result obtained from UV–vis diffuse reflectance spectra (Fig. 4b) which the band gap was continually declined with the Eu^{3+} doping concentration

increasing. Because the DFT simulation was on the base of fixing crystal structure, the structure disordering was not considered in such model. Thus the deviation, that is, the red shift was observed for the band gap of LaOCl:Eu^{3+} nanostructures, should be induced by the lattice strain originating from the structure misplacement. Several references had reported the lattice strain could effectively influence on the electronic properties of nanostructures, and further effect on the band structures.[23, 45-47]

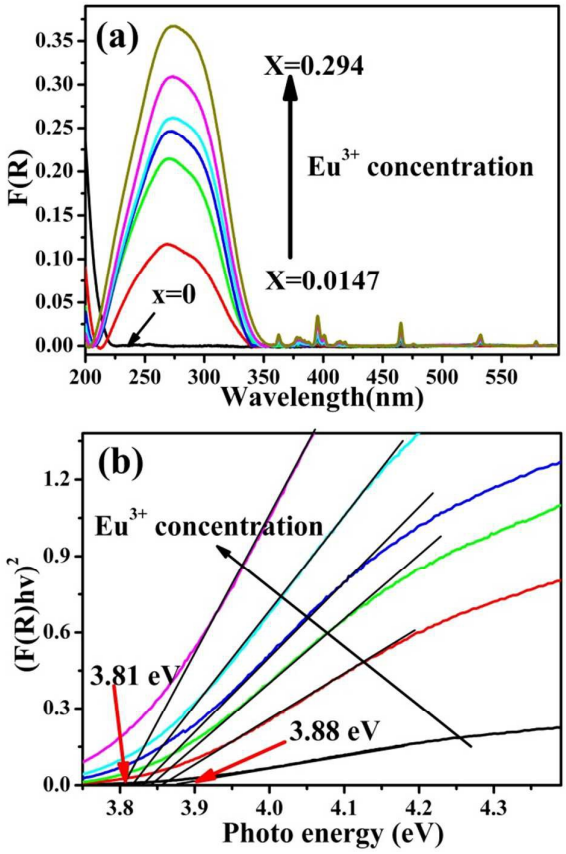

Fig. 6 UV-vis reflectance spectra (a) and band gap (b) of LaOCl:Eu^{3+} nanodisks.

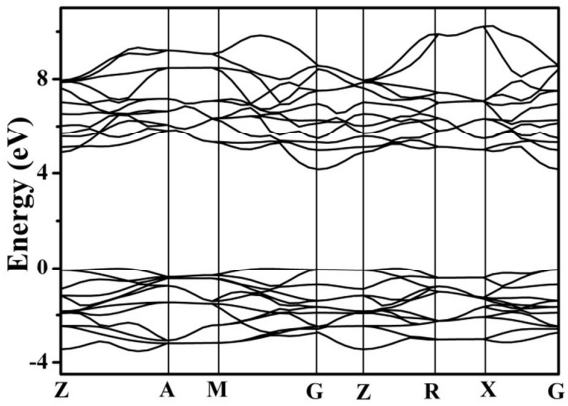

Fig. 7 Band structures for pure LaOCl nanodisks.

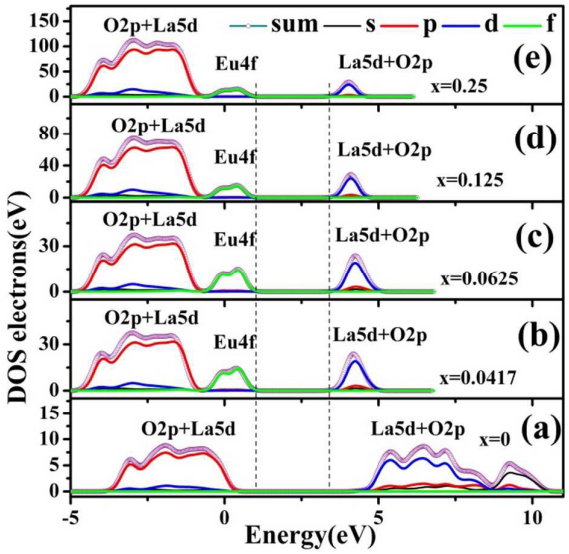

Fig. 8 Density of states (DOS) of pure LaOCl and doping models.

FT-IR spectra of Eu^{3+} doped LaOCl were shown in Fig. 9. The broad band at about 3400 and 1650 cm^{-1} were belonged to the typical H-O vibration and stretch mode of absorbed H_2O layer on the sample surface, respectively. The existence of water may arised from residual water in the sample and/or absorbed moisture during the measurement. The presence of a band at around 510 cm^{-1} was observed, which belonged to the stretching vibration of La-O.[48] As seen in the inset image of Fig. 9, the La-O vibration band shifted to higher wavenumbers with the Eu^{3+} content increasing, which assigned to the structural changes due to Eu^{3+} doping.[49] As mentioned above XRD results, the introduction of Eu^{3+} in LaOCl lattice led to the bond length shrinkage and lattice contraction. Subsequently, the force constant should strengthen and the vibration band should shift to high wavenumber.[50] In this sense, structure shrinkage induced by Eu^{3+} doping effect is a likely cause for the blue shift of the phonon peak of La-O vibration mode.

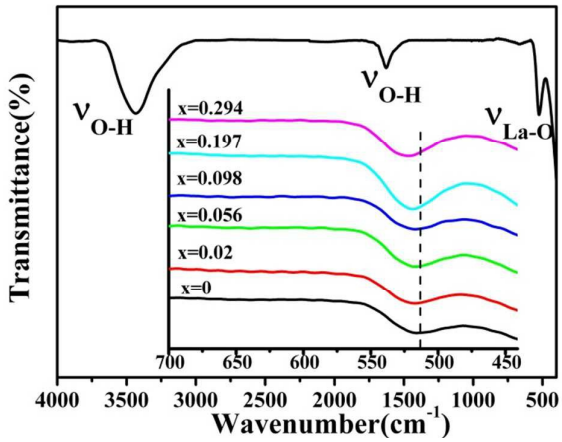

Fig. 9 FT-IR spectra of LaOCl:Eu^{3+} nanodisks (x = 0.056), (inset) Enlarged FT-IR spectra for LaOCl:Eu^{3+} nanodisks in a narrowed wavelength.

The luminescent properties of Eu^{3+} doped LaOCl nanodisks were performed. As seen in the excitation spectra (Fig. 10), a broad peak centered at 270 nm was observed. It was attributed to the Eu-O charge transfer (CT) band, which arised from the transition of 2p electrons of O^{2-} to the empty 4f orbital of Eu^{3+} ions. It was interesting noted that the main peak location of the CT band in the LaOCl:Eu^{3+} crystals (x = 0.294) of 312 nm was slightly red shift in comparison with that of 296 nm in the LaOCl:Eu^{3+} crystals（x = 0.015). It is well-known that the CT energy depended strongly on the nature of the surrounding ions.[50] The effect of the surrounding factors can be numerically accounted for in the spectroscopic behavior through the so-called environmental factor (h_e), which was characteristic for each host lattice. The energy relative to the maximum of the CT band was exponentially related to the environmental factor, as pointed out in equation (3): [51]

$$E_{\mathrm{CT}} = A + Be^{-k\hbar_e} \quad (3)$$

where A = 2.804, B = 6.924, and k = 1.256 for Eu^{3+} ion. With the Eu^{3+} doping concentration increasing from 0.015 to 0.294 in our LaOCl:Eu^{3+} system, the calculated environmental factors (h_e) obtained by equation (3) range from 1.281 to 1.416. The influence factors of crystal structural factors included the covalence, coordination number, bond polarizability, and cation charge. [52] To determine which one is the mainly factors for our LaOCl:Eu^{3+} system, the above influence factors will be exclude one by one. In fact, the form of the CT band comes from two factors: 5d energy level of Eu^{3+} and valence electron energy level of the ligand O^{2-}.[51] For our research system, when the La^{3+} ions was substituted by different ration Eu^{3+} ions into LaOCl host matrix, the coordination number of La or Eu element was not almost altered, because (1) the ions radius of Eu^{3+} is 1.066 Å, close to 1.16 Å of La^{3+} ions; (2) the charge of La and Eu in crystal is +3, which is exactly the same. Thus, the coordination number, the covalence and ion charge did not include into the significantly affection for the environmental factor. Considering the polarizable effect, the electronegativity should be further analyzed during Eu^{3+} ions substituted La^{3+} ions in the LaOCl host matrix. Because the electronegativity of Eu element is 1.19, being little larger than that of 1.11 for La element, it may not result in an increase of the effective charge surrounding. Consequently, the charge rearrangement was scarcely possible happened. Thus, the polarizable environment effect should be also ignored. The shrinkage of the La-O vibration band with the Eu^{3+} content increasing was observed from FT-IR spectra of LaOCl:Eu^{3+} nanodisks (Fig.9). The covalence of Eu–O bond in the crystals was enhanced a little bit with Eu^{3+} ions doped into LaOCl host matrix increases.[52] By the above accounts, it is proposed that the CT band shifted to lower energy due to the structure variation. In addition, a series of sharp peaks in excitation spectra from 300 to 500 nm were also observed, which correspond to f-f transitions within the Eu^{3+} $4f^6$ electron configuration transitions of Eu^{3+}, respectively. Due to forbidden by the selection rules, the intensities of the peaks were relatively low.[54, 55]

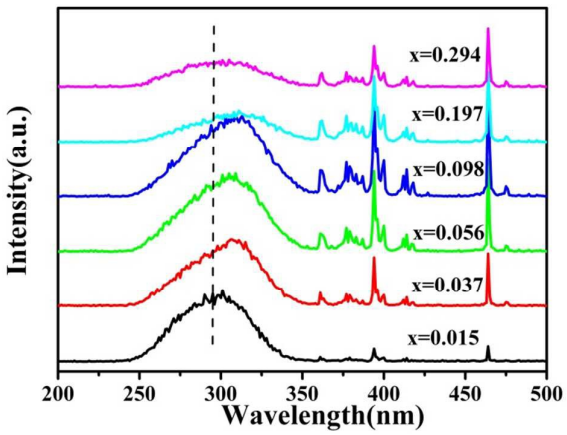

Fig. 10 Excitation spectra (λ_{em} = 615 nm) of Eu^{3+} doped LaOCl nanodisks.

In order to know details about the change of luminescent property on Eu^{3+} doping in the LaOCl matrix, emission spectra were performed. Upon excitation at 277 nm, a summary of the photoluminescence (PL) profile of doped samples was presented in Fig. 11. The pure sample was inertia on the luminescent property. $^5D_0$-^7F_J (J = 1, 2, 3, 4) emission lines of Eu^{3+} could be found for the Eu^{3+} doped LaOCl nanodisks. Among the emission peaks of Eu^{3+}, the electron-dipole transition $^5D_0$-$^7F_2$ (615 nm) is the most prominent group, which yields a red color emission. Furthermore, the other relatively weak emissions belonged to the characteristic peak of the Eu^{3+} f-f transitions were presented as well, which can be assigned to the $^5D_0 \rightarrow {}^7F_1$, $^5D_0 \rightarrow {}^7F_3$, and $^5D_0 \rightarrow {}^7F_4$ transitions in the visible region centered at 590, 650, and 701 nm, respectively.[56]

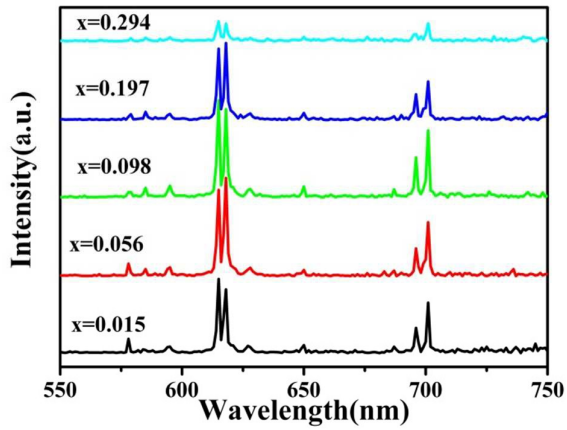

Fig. 11 Emission spectra of LaOCl:Eu^{3+} nanodisks.

With the increase Eu^{3+} doping concentration, the emission intensities of the Eu^{3+}-doped LaOCl sample increased gradually. Because the increase of Eu^{3+} concentration led to the increase of luminescence centre, it would enhance the emission intensity. However, when the Eu^{3+} content increased to x = 0.098, the emission intensity increased to maximum value, and then decreased. It is reported that the concentration quenching effect would alter the emission

intensity. [57] The concentration quenching might be undermined by the basis of following two factors: exchange-type interactions, or multipole-multipole interactions.[57] The exchange-type interaction is responsible for energy transfer of forbidden transition. Eu^{3+} ions 4f -4f transition is inhibited radiative transition, but exchange transition is generally limited to interaction between rare earth ions in the nearest neighbour or next nearest neighbour. The intensity emission of the rare earth ions is little affected by exchange interaction.[58] Thus, the energy transferred by the multipole-multipole interactions would take into consideration for our system, which belonged to non-radiative pattern.[57] It is strange that the emission intensity steeply declined to minimum value with Eu^{3+} doping concentration increased. Thus, it was inferred concentration quench effect was not the only cause in the present system. Aumer et al.[59] reported that the luminescent intensity of AlInGan/ InGaN decreased with increasing tensile strain. It was indicated that the non-radiative relaxation pathway increased with increasing lattice strain. Thus, we believe the lattice strain will also decrease the emission intensity for LaOCl:Eu^{3+} decreased, as shown in Fig. 12. Based on the analysis results, lattice strain and doped concentration played an important role in tuning the efficiency of the luminescent properties of doped nanodisks. In addition, it was reported that the OH ions can act as the quenchers centres to the luminescence of rare earth ions through multiphonon relaxation.[60, 61] The quantum efficiency for the luminescent materials should be related closely to the existence of water molecule adsorbed on the surface of sample, since it was inevitable to introduce OH ions which were easily coordinated to the rare earth ions. For our system, because the samples were prepared in wet chemical routes and followed to calcine at 600 °C for 4 h, the surfaces of samples were absorbed litter water molecule, confirmed by the result of TG analysis (Fig. S4). Meanwhile, the contents of water absorbed the samples were ignored in 35 to 400 ºC with the doping Eu^{3+} concentration increasing. Therefore, the influence of OH ions on the quantum efficiency in our system was not considered.

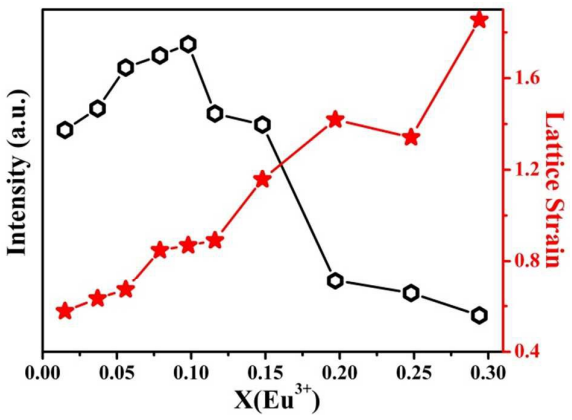

Fig. 12 The relation of emission intensity, lattice strain as a function the Eu^{3+} dopant level.

Apart from the luminescent property, another important characteristic is the luminescent lifetime of the emitting system. Luminescent decays for $^5D_0$ level of Eu^{3+} in LaOCl (x = 0.015, 0.056, 0.098, 0.148, 0.197 and 0.294) were shown in Fig. 13, when excitation and emission wavelengths were fixed at 395 and 615 nm, respectively. To understand the behavior of luminescent decay, we tried to fit the decay data. All the curves of the decay time of the as-obtained samples could be well fitted by using double exponential function: [62]

$$I = I_0 + A_1 e^{-t/\tau_1} + A_2 e^{-t/\tau_2} \quad (4)$$

where A_1 and A_2 are intensities at different time intervals, τ_1 and τ_2 are the two different lifetimes of Eu^{3+} ions, the lifetime (τ_1) associated with diffusion and energy transfer rate was shorter than another one (τ_2). It is assumed that there are two different sites in crystals, one is the inner part (core), that could be more ordered, and the other is the perturbed, less ordered layer near the surface. Eu^{3+} ions occupying the inner part have a longer lifetime than those in the less ordered layer near the surface. The τ_1 may be attributed to the surface crystals, while τ_2 to the relatively deeper core.[63] The values of lifetime (τ_1 and τ_2) for the Eu^{3+} ions along with their relative percentages were given in Table S4. As illustrated in Table S4, when the Eu^{3+} doping concentration was low, the shorter lifetime (τ_1) contributed to the longer lifetime (τ_2). However, when Eu^{3+} doping concentration was 0.098, the contributed of τ_1 to minimum was 42.1%. It is means that the number of Eu^{3+} occupied the surface site was declined, that is, the non-radiation loss was relatively low. So, it was expected the strongest emission intensity was obtained when the Eu^{3+} doping concentration was 0.098.

As shown in inset image of Fig. 13, the quantum efficiency was as high as 87.4% when the Eu^{3+} content was 0.037. It was indicated that the material of LaOCl:Eu^{3+} nanodisks had an excellent luminescent property. Meanwhile, the ratios of the intensity of $^5D_0$-$^7F_2$ to $^5D_0$-$^7F_1$ (R/O) for LaOCl:Eu^{3+} nanodisks were about 10, when the Eu^{3+} doping concentration was smaller than 0.148 (Table S5). The CIE (Commission International de l´Eclairage, France) chromaticity coordination of the samples with different Eu^{3+} doping concentration were calculated to be about x = 0.60, y = 0.34 (Table S5). Therefore, LaOCl:Eu^{3+} material should be served as a good red phosphor.

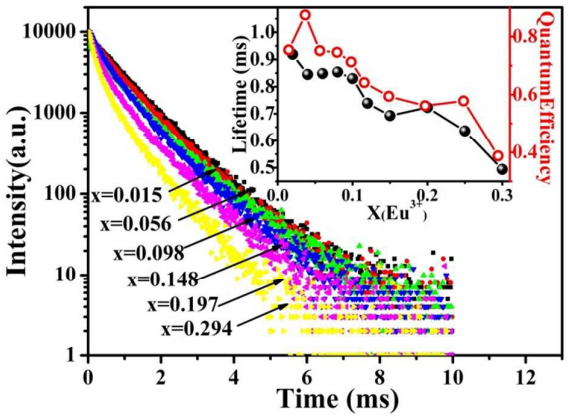

Fig. 13 Lifetime decay curves of LaOCl:Eu^{3+} nanodisks. (Inset) the lifetime and quantum efficiency as a function the Eu^{3+} dopant level.

Conclusions

In summary, Eu^{3+} doped LaOCl nanodisks have been successfully prepared. The detailed structures for the LaOCl:Eu^{3+} nanodisks were comprehensively characterized. It is found that the lattice parameters (a and c) and lattice volume of Eu^{3+} doped LaOCl nanodisks have been influenced by Eu^{3+} doping, and then lattice strain was generated by the resulting lattice distortion. Further, the detailed electronic structures for LaOCl:Eu^{3+} nanodisks were investigated by UV-vis spectra and theoretical simulation calculation. The doping effect and lattice strain leads to the reduction of the band gap. The excitation band positions shift to low energy due to the covalence enhanced of Eu-O band. By doping with Eu^{3+} ions in LaOCl host matrix, the samples exhibit highly efficient luminescent properties. The quantum efficiency is up to 87.4%, when the Eu^{3+} doping concentration is 0.037. The finding in this work is important, which provide a chance to study the relation of lattice structure and luminescent property.

Acknowledgements

This work is financially supported by the National Natural Science Foundation of China (Grants 21267041, 21367018), the Project of Scientific and Technological Innovation Team of Inner Mongolia University (12110614), the Science Research Foundation of the Inner Mongolia University of Technology (ZS201110, X200811).

References

1 G. G. Li, Z. Y. Hou, C. Peng, W. X. Wang, Z. Y. Cheng, C. X. Li , H. Z. Lian and Jun Lin, *Adv. Funct. Mater.* 2010, **20**, 3446–3456.
2 T. Konishi, M. Shimizu, Y. Kameyama and Kohei Soga, *J Mater Sci: Mater Electron*, 2007, **18**, S183–S186.
3 W. S. Yu, Q. L. Kong and J. X. Wang, *J Mater Sci: Mater Electron*, 2014, **25**, 46–56.
4 S. S. Lee, H. I. Park, C. H. Joh and S. H. Byeon, *J. Solid State Chem.*, 2007, 180, 3529–3534.
5 M. Guan, L. F. Mei, Z. H. Huang, C. X. Yang, Q. F. Guo and Z. G. Xia, *Infrared Phys. Techn.*, 2013, **60**, 98–102.
6 S. S. Lee, C. H. Joh and S. H. Byeon, *Mater. Sci. Eng. B,* 2008, **151**, 163–168.
7 K. R. Kort and S. Banerjee, *Inorg. Chem.*, 2011, **50**, 5539–5544.
8 G. G. Li, C. X. Li, C. M. Zhang, Z. Y. Cheng, Z. W. Quan, C. Peng and J. Lin, *J. Mater. Chem.*, 2009, **19**, 8936-8943.
9 J. Hölsä, E. J. Kestilä and K. Koski, *J. Alloys Compd.*, 1995, **225(1–2)**, 651-656.
10 Z. G. Xia, J. Li, Y. Luo and L. B. Liao, *J. Am. Ceram. Soc.*, 2012, **95(10)**, 3229–3234.
11 D. Kim, J. Jang, S. I. Ahn, S. H. Kim and J. C. Park, *J. Mater. Chem. C*, 2014, **2**, 2799-2805.
12 M. L. Zhao, G. S. Li, J. Zheng, L. P. Li, H. Wang and L. S. Yang, *CrystEngComm*, 2011, **13**, 6251-6257.
13 C. C Fu, G. S. Li, M. L. Zhao, L. S. Yang, J. Zheng and L. P. Li, *Inorg. Chem.*, 2012, **51**, 5869−5880.
14 A. Kar, S. Kundu, and A. Patra, *J. Phys. Chem. C*, 2011, **115**, 118–124.
15 Q. L. Kong, J. X. Wang, X. T. Dong, W. S. Yu and G. X. Liu, J Mater Sci, 2014, 49, 2919–2931.
16 Q. L. Kong, J. X. Wang, X. T. Dong, W. S. Yu and G. X. Liu, J Mater Sci: Mater Electron, 2013, 24, 4745–4756.
17 W. S. Yu, Q. L. Kong, J. X. Wang, X. T. Dong and G. X. Liu, J Mater Sci: Mater Electron, 2014, 25, 46–56.
18 Q. L. Kong, J. X. Wang, X. T. Dong, W. S. Yu and G. X. Liu, , Journal of Experimental Nanoscience, 2015, 10, 947-964.
19 P. Ghosh and A. Patra, *J. Phys. Chem. C,* 2008, **112**, 19283–19292.
20 D. Sreekantha Reddy, B. Kang, S. C. Yu, K. R. Gunasekhar, K. Narasimha Rao and P. Sreedhara Reddy, *J. Appl. Phys.*, 2008, **104**, 013532.
21 Y. Park, C. Koo, H. Y. Chen, A. Han and D. H. Son, *Nanoscale*, 2013, **5**, 4944–4950.
22 N. J. J. Johnson and F. C. J. M. van Veggel, *ACS Nano*, 2014, **8 (10)**, 10517–10527.
23 A. M. Smith, A. M. Mohs and S. Nie, *Nat. Nanotechnol.*, 2009, **4**, 56-63.
24 E. Klimešová, K. Kůsová, J. Vacík, V. Holý and I. Pelant, *J. Appl. Phys.*, 2012, **112**, 064322.
25 S. Sadhu and A. Patra, *J. Phys. Chem. C*, 2012, **116**, 15167−15173.
26 P. Ghosh, E. de la Rosa, J. Oliva, D. Solis, A. Kar and A. Patra, *J. Appl. Phys.*, 2009, **105**, 113532.
27 W. L. Ji, X. Y. He, W. X. Cheng, P. S. Qiu, X. Zeng, B. Xia and D. Wang, *Ceram. Int.*, 2015, **41**, 1950–1956.
28 G. Srinet, R. Kumar and V. Sajal, *Ceram. Int.*, 2014, **40**, 4025–4031.
29 R. Shi, G. L. Huang, J. Lin and Y. F. Zhu, *J. Phys. Chem. C* 2009, **113**, 19633−19638.
30 B. H. Toby, *J. Appl. Cryst.*, 2001, **34**, 210-213.
31 Y. G. Su, L. M. Peng, J. W. Guo, S. S. Huang, L. Lv and X. J. Wang, *J. Phys. Chem. C*, 2014, **118**, 10728−10739.
32 R. K. Hailstone, A. G. DiFrancesco, J. G. Leong, T. D. Allston and K. J. Reed, *J. Phys. Chem. C*, 2009, **113**, 15155−15159.
33 G. S. Li, J. Boerio-Goates, B. F. Woodfield and L. P. Li, *Appl. Phys. Lett.*, 2004, **85**, 2059−2061.
34 Y. G. Su, G. S. Li, X. J. Wang and L. P. Li, *J. Lumin.*, 2012, **132**, 1407–1413.
35 Y. G. Su, L. C. Hou, C. F. Du, L. M. Peng, K. Guan and X. J. Wang, *RSC Adv.*, 2012, **2**, 6266–6273.
36 Y. G. Su, L.P. Li and G.S. Li, *Chem. Mater.*, 2008, **20**, 6060–6067.
37 D. Kim, J. Jang, S. I. Ahn, S. H. Kim and J. C. Park, *J. Mater. Chem. C*, 2014, **2**, 2799–2805.
38 M. V. Sofianou, M. Tassi, V. Psycharis, N. Boukos, S. Thanos, T. Vaimakis, J. G. Yu and C. Trapalis, *Appl. Catal. B*, 2015, **162**, 27–33.
39 Y. G. Su, X. Xin, Y. F. Wang, T. T. Wang and X. J. Wang, *Chem. Commun.*, 2014, **50**, 4200-4202.
40 L. P. Li, G. S. Li, J. Xiang, R. L. Smith Jr. and H. Inomata, *Chem. Mater.* 2003, **15**, 889-898.
41 G. K. Williamson and W. H. Hall, *Acta Metall.*, 1953, **1**, 22.
42 D. Kim, S. Park, S. Kim, S. G. Kang and J. C. Park, *Inorg. Chem.* 2014, **53**, 11966−11973.
43 J. L. Hu, H. M. Li, C. J. Huang, M. Liu, X. Q. Qiu，*Appl. Catal. B*, 2013, **142– 143**, 598– 603.
44 H. H. C. Lai, T. Basheer, V. L. Kuznetsov, R. G. Egdell, R. M. J. Jacobs, M. Pepper and P. P. Edwards, *J. Appl. Phys.*, 2012, **112**, 083708.
45 X. Q. Qiu, Masahiro Miyauchi, H. G. Yu, Hiroshi Irie and Kazuhito Hashimoto, *J. Am. Chem. Soc.*, 2010, **132**, 15259–15267.

46 D. I. Bazhanov, I. V. Mutigullin, A. A. Knizhnik, B. V. Potapkin, A. A. Bagaturyants, L. R. C. Fonseca and M. W. Stoker, *J. Appl. Phys.*, 2010, **107**, 083521.
47 Z. M. Zhu, G. Ouyang and G. W. Yang, *J. Appl. Phys.*, 2010, **108**, 083511.
48 L.M. Sharaf El-Deen, M.S. Al Salhi and M.M. Elkholy, *J. Alloys Compd*., 2008, **465**, 333–339.
49 Q. L. Chen, H. Wang, Q. W. Wang and Q. P. Chen, *J. Non-Cryst. Solids*, 2014, **404**, 145–150.
50 M. Ghosh, N. Dilawar, A. K. Bandyopadhyay and A. K. Raychaudhuri, *J. Appl. Phys.*, 2009, **106**, 084306.
51 L. Li and S. Y. Zhang, *J. Phys. Chem. B*, 2006, **110**, 21438-21443.
52 J. C. Batista, P. C. de Sousa Filho and O. A. Serra, *Dalton Trans.*, 2012, **41**, 6310-6318.
53 H. Q. Yu, H. W. Song, G. H. Pan, S. W. Li, Z. X. Liu, X. Bai, T. Wang, S. Z. Lu and H. F. Zhao, *J. Lumin.*, 2007, **124**, 39–44.
54 Y. P. Fang, A. W. Xu, R. Q. Song, H. X. Zhang, L. P. You, J. C. Yu and H. Q. Liu, *J. Am. Chem. Soc.*, 2003, **125**, 16025-16043.
55 L. Lv, J. Z. Wang, W. Wang and L. M. Han, *J. Alloys Compd.*, 2015, **635**, 25–33.
56 Y. P. Fang, A. W. Xu, R. Q. Song, H. X. Zhang, L. P. You, J. C. Yu and H. Q. Liu, *J. Am. Chem. Soc.*, 2003, **125**, 16025-16034.
57 Y. Zhang, X. J. Li, K. Li, H. Z. Lian, M. M. Shang and J. Lin, *J. Mater. Chem. C*, 2015, **3**, 3294—3303.
58 L. G. Van Uitert, *Energy Transfer Interactions*, 1967, **114**, 1048-1053.
59 M. E. Aumer, S. F. LeBoeuf, S. M. Bedair, M. Smith, J. Y. Lin and H. X. Jiang, *Appl. Phys. Lett.*, 2000, **77**, 821-823.
60 X. C. Jiang, C. H. Yan, L. D. Sun, Z. G. Wei and C. S. Liao, *J. Solid State Chem., 2003,* **175**, 245 – 251.
61 Y. G. Su, L.L. Li and G.S. Li, *Cryst. Growth Des.,* 2008, **8**, 2678-2683.
62 T. Grzyb and S. Lis, *Inorg. Chem.*, 2011, **50**, 8112–8120.
63 C. J. Yim, S. Unithrattil, W. J. Chung and W. B. Im, *Mater. Charact.*, 2014, **95**, 27-35.